Composites Part B 225 (2021) 109269

Contents lists available at ScienceDirect

Composites Part B

journal homepage: www.elsevier.com/locate/compositesb

Fabrication of melamine trimetaphosphate 2D supermolecule and its superior performance on flame retardancy, mechanical and dielectric properties of epoxy resin

Peifan Qin [a], Deqi Yi [a,*], Jianwei Hao [a], Xinming Ye [a,b], Ming Gao [c], Tinglu Song [d]

[a] National Engineering Research Center of Flame Retardant Materials, School of Materials Science and Engineering, Beijing Institute of Technology, No. 5 South Zhongguancun Street, Haidian District, Beijing, 100081, PR China
[b] School of Chemistry and Chemical Engineering, Beijing Institute of Technology, No. 5 South Zhongguancun Street, Haidian District, Beijing, 100081, PR China
[c] School of Chemical and Environmental Engineering, North China Institute of Science and Technology, Yanjiao Beijing, 101601, PR China
[d] Experimental Center of Advanced Materials School of Materials Science & Engineering, Beijing Institute of Technology, No. 5 South Zhongguancun Street, Haidian District, Beijing, 100081, PR China

ARTICLE INFO

Keywords:
Melamine
Sodium trimetaphosphate
Supermolecule
Epoxy resin
Flame retardancy
Mechanical property
Dielectric property

ABSTRACT

To improve the flame retardancy, mechanical and dielectric properties of epoxy resin (EP), a novel two-dimensional (2D) supermolecule, melamine trimetaphosphate (MAP), is successfully synthesized using melamine (MA) and sodium trimetaphosphate (STMP) in aqueous solution. Its chemical, crystalline structure and thermal stability are thoroughly characterized by Fourier transform infrared (FTIR), nuclear magnetic resonance (NMR), X-ray diffraction (XRD), scanning electron microscope (SEM), transmission electron microscope (TEM), atom force microscope (AFM) and thermo-gravimetric analysis (TGA) techniques. Then EP-MAP composites are prepared, and their morphologies are assessed by SEM, thermal stability by TGA, fire retardancy by limiting oxygen index test (LOI), vertical burning standard test (UL-94), and cone calorimeter tests, mechanical properties by stress strain tests, and dielectric properties by impedance analyzer. The results show that the MAP layers are formed by a 3:1 combination of MA and STMP rings via intermolecular hydrogen bonding. The MAP sheets with a thickness of around 2 nm show high thermal stability. Compared to pure EP, the thermal stability of EP-MAP is improved, and EP-MAP composite can achieve 30.0% of LOI value and UL-94 V-0 rating with only 4% MAP. Meanwhile its peak of heat release rate is reduced by 65.6% and the smoke release is highly suppressed in the cone calorimeter test. The typical intumescent flame retardancy effect and phosphorus-nitrogen (*P*–N) effect during the combustion of EP-MAP are demonstrated by X-ray photoelectron spectroscopy (XPS) and thermogravimetric analyzer coupled with Fourier transform infrared analysis of evolving products (TGA-FTIR). Due to the uniform dispersion of MAP in EP matrix, the mechanical and dielectric properties of EP-MAP are also significantly enhanced.

1. Introduction

Nowadays, epoxy resins (EP) have been applicated in electronics, aerospace parts, petrochemicals, and manufacturing due to the good adhesion, chemical resistance, and mechanical properties [1–6]. With the rapid development of electronics and electrical appliances (E&E), more and more enhanced physical and chemical properties are required for EP [7,8], such as thermal stability, flame retardancy, mechanical and dielectric properties. At present, tetrabromobisphenol-A (TBBPA) is the most used flame retardant for EP in E&E. But the potential toxicity of TBBPA pushed researchers to pursue suitable halogen-free flame retardants [9–11], such as polyhedral oligomeric silsesquioxane (POSS) [12,13], ammonium polyphosphate (APP) [14], dihydrooxaphosphaphenanthrene (DOPO) and its derivatives [15,16]. Although the phosphorus-containing intumescent flame retardant (IFR) system shows good flame retardancy for EP, it is usually based on the loss of other properties due to poor compatibility and dispersion, as well as poor water resistance and efficiency of the flame retardancy [17,18]. Therefore, solving these problems become emergency to the application of phosphorus-containing flame retardants in EP [19].

* Corresponding author.
E-mail address: yidq@bit.edu.cn (D. Yi).

https://doi.org/10.1016/j.compositesb.2021.109269
Received 16 June 2021; Received in revised form 18 August 2021; Accepted 29 August 2021
Available online 31 August 2021

Supermolecule self-assembled formed by non-covalent bonds among molecules have emerged as a promising technique for various applications [20,21]. In particular, hydrogen bonding is widely used for the formation of supermolecule aggregates because of the strong directional property, which simplifies the design of complementary subunits for recognition and binding [22,23]. Based on the intermolecular hydrogen bonding, many supermolecules have been synthesized and show a good performance for improving the flame retardancy of polymers [24,25]. For example, melamine cyanurate (MCA), as a typical 2D supermolecule flame retardant, has been widely investigated until now [26]. Recently, Pingan Song et al. reported that $Ti_3C_2T_x$@MCA nanohybrid was prepared via hydrogen bonding interactions, showing outstanding properties in thermoplastic polyurethane [27]. And Deqi Yi et al. synthesized an interdigitated crystalline MMT-MCA [28]. In addition, some supermolecule flame retardants based on APP and melamine-phytate have also been developed [29,30]. It is noticed that all these designed supermolecules do not contain all components of IFR. So, in previous work, we designed and synthesized poly (diallyldimethylammonium) and polyphosphate (PAPP) polyelectrolyte complex as a "all-in-one" IFR, which shows good flame retardancy, but poor dispersion and mechanical properties due to uncontrollable 3D network structure of the PAPP [31,32]. So, we believe that a "all-in-one" IFR with controllable structure, especially 2D structure, will improve both the physical and chemical properties of EP.

In this paper, a novel 2D supermolecule, melamine trimetaphosphate (MAP), is successfully synthesized using melamine (MA) and sodium trimetaphosphate (STMP) in aqueous solution. Then EP-MAP composites are prepared. The results show that MAP layers with thickness at 2 nm are formed by 3:1 combination of MA and STMP molecules via intermolecular hydrogen bonding. Compared to pure EP, the thermal stability of EP-MAP is improved, and EP-MAP can achieve 30.0% of LOI value and UL-94 V-0 rating with only 4% MAP. Meanwhile its peak of heat release rate is reduced by 65.6% and the smoke release is highly suppressed. The typical intumescent flame retardancy effect and phosphorus-nitrogen (*P*–N) effect are exhibited by the analysis of char. Moreover, the mechanical and dielectric properties of EP are also enhanced due to the uniform dispersion of MAP in EP matrix. MAP, as an "all-in-one" IFR, can effectively improve the collision probability between acid source, charring agent and blowing agent, thereby effectively increasing the flame retardancy. Meanwhile, the controllable 2D supermolecule structure endows MAP good dispersion in EP. With slight addition of MAP, EP-MAP composites show outstanding flame retardancy, mechanical and dielectric properties, which outperforms other fillers in properties improvement.

2. Experimental section

2.1. Materials

MA, STMP and HCl are purchased by Beijing Chemical Reagent Company, China. Diglycidyl ether of bisphenol A (DGEBA, E−44, equivalent = 0.44 mol/100 g) is purchased by Feicheng Deyuan Chemicals Co., Ltd. 4,4-diaminodiphenylsulphone (DDS, > 98.0%), is purchased from the Tianjin Guangfu Fine Chemical Research Institute. Deionized water is used during the preparation.

2.2. Preparation of MAP and EP-MAP composites

MA powder (12.6 g) is added into 500 mL of deionized water and dissolved at 90 °C in three-necked flask. Then 100 mL of STMP solution at 3.3×10^{-1} M is slowly added to the MA solution with intensive agitation at 90 °C for 1 h. Subsequently, HCl solution with pH = 1 is dropwise added to reach an equimolar amount with MA. Then the mixture is continually stirring for 1 h. Finally, the white solid product can be obtained by filter, and then is washed by deionized water and dried at 100 °C in a vacuum oven. The yield of MAP is about 96%. The obtained MAP is milled and screened through 100-mesh sieves. The solubility of MAP is determined as 0.043 g per 100 g water at 20 °C.

DGEBA (E44) is added to a three-necked flask with mechanical stirring at 140 °C for 30 min, then the MAP is added and stirring for 1 h to disperse it sufficiently. Finally, DDS is added and stirred for 15 min. The resulting liquid mixture is rapidly transferred into a mold and cured at 180 °C for 4 h. Pure EP is also prepared using a similar process. The synthetic route of MAP and curing process of EP-MAP composites are presented in Fig. 1. The components of EP composites are listed in Table 1.

2.3. Characterization

Fourier transform infrared (FTIR) spectra are obtained on a Nicolet 6700 spectrometer in detection mode using diamond as the cell material. The spectra are collected in 32 scans with a spectral resolution of 1 cm^{-1} using the attenuated total reflection (ATR) method.

The ^{31}P NMR spectrum of STMP is conducted on a Bruker Advance 600 NMR spectrometer and D_2O is used as the solvent. The ^{31}P and ^{1}H solid-state magic-angle spinning NMR experiments are performed on JNM-ECZ600R spectrometer at a resonance frequency of 600 MHz. The spectra are recorded with spinning rate of 15 kHz with a 3.2 mm probe at room temperature. The experiments are performed with a delay time of 5 s. Scan number: 200 scans.

The structure-related characterizations are performed by X-ray diffraction (XRD) with a rotating anode X-ray diffractometer (Japan Rigaku Miniflex 600) equipped with a Cu *Kα* radiation source (λ = 0.1542 nm). The samples are scanned in the 2θ values ranging from 2° to 50° with a step size of 0.02° and a scanning rate of $2^{\circ}\cdot min^{-1}$.

The true density of MAP sample is measured by the Ultrapycnometer 1000 and its five-station sibling the Pentapycnometer.

Scanning electron microscope (SEM) images and corresponding energy-dispersive X-ray (EDS) spectra are collected on a FEI Quanta 650 FESEM at an accelerating voltage of 10 kV.

Transmission electron microscope (TEM) images and corresponding selected area electron diffraction (SAED) are collected on a FEI Tecnai G2 F30 TEM with an accelerating voltage of 300 kV.

Atom force microscope (AFM) images are recorded on Asylum Research Cypher S (Oxford Instruments) with tapping mode.

Thermo-gravimetric analysis (TGA) is performed on a Netzsch 209 F1 thermal analyzer under a 50 mL/min nitrogen flowing atmosphere at a heating rate of 10 °C/min from 40 to 800 °C.

A Netzsch DSC 214 instrument (Netzsch, Germany) under a nitrogen gas flow (60 mL/min) is used to investigate the endothermic process. The samples are first heated from 40 to 240 °C, then cooled to 40 °C and reheated to 240 °C at a heating rate of 10 °C/min. The second heating thermograms are recorded.

The limiting oxygen index (LOI) is obtained using the standard GB/T 2406–93 procedure. An LOI instrument (Rheometric Scientific Ltd.) is used on barrel-shaped samples with dimensions of $100 \times 6.5 \times 3$ mm^3.

The UL-94 vertical burning test is conducted on a CZF-5A type instrument (Jiangning Analysis Instrument Co.) on the basis of the America National UL-94 test ASTM D 3801 with samples dimensions of $125.0 \times 13.0 \times 3.2$ mm^3.

The cone calorimeter test is performed with a fire testing technology apparatus (FTT) under 50 kW/m^2 external radiant heat flux conforming to ISO 5660 protocol. The specimen ($100 \times 100 \times 3$ mm^3) is measured horizontally without any grids. Characteristic results are reproducible within ±10% and the results are the average for three measurements.

The X-ray photoelectron spectroscopy (XPS) spectra are obtained by PHIQUANTERA-II SXM at 15 kV × 25 W under a vacuum lower than 10^{-6} Pa.

Thermo-gravimetric analysis (Netzsch 209 F1) is coupled with Fourier-transform infrared spectroscopy (Nicolet 6700) under nitrogen atmosphere from 40 °C to 800 °C at a heating rate of 20 °C/min. The sample weight is 5–10 mg for each test.

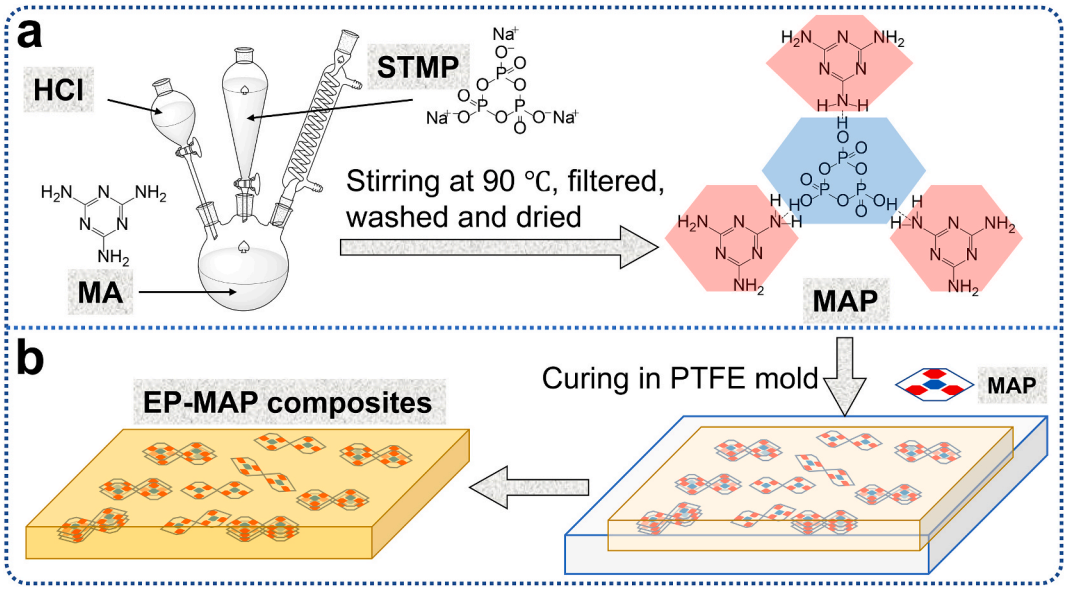

Fig. 1. Synthesis route (a) of MAP and scheme of curing process (b) for EP-MAP composites.

Table 1
Components of EP-MAP composites.

Samples	Components by weight			
	EP (%)	MAP (%)	P (%)	N (%)
EP	100	0	0	0
EP-MAP-1%	99	1	0.15	0.41
EP-MAP-2%	98	2	0.30	0.82
EP-MAP-3%	97	3	0.45	1.23
EP-MAP-4%	96	4	0.60	1.64

The flexural properties are measured using an DXLL-5000 testing machine (Shanghai D&G Measure Instrument Co., Ltd.) with a three-point bending fixture at a crosshead speed of 5 mm/min at room temperature. The dimensions of the specimens are 100 × 15 × 4 mm^3 and the span to thickness ratio is set at L/d = 16:1 according to the GB/T 2570–1995. At least five specimens are tested for each sample to obtain averages of the bending strength and strain at break.

The relative dielectric constant and dielectric loss of samples is measured by an impedance analyzer (Wayne Kerr 1J6520B, UK) in a frequency range of 1 kHz–10 MHz. All measured samples have a thickness of 2 mm and diameter of 50 mm.

3. Results and discussion

3.1. The morphologies of MAP

Fig. 2 shows the FTIR spectra of MAP, STMP, and MA. For MA, the peaks at 3470 and 3415 cm^{-1} are attributed to the symmetric and asymmetric *N*–H stretching of NH_2 non–hydrogen bonded groups, and the peaks centered at 3318 and 3120 cm^{-1} are assigned to the *N*–H stretching of amino groups hydrogen bonded of MA molecules [28]. The peaks at 1624, 1525, 1427, 1017 and 810 cm^{-1} correspond to NH_2 deformation vibration, C═N and *C*–N stretching vibrations, breathing and bending of MA ring, respectively [33,34].

For STMP, the peaks at 1290, 1265 and 1097 cm^{-1} belong to P═O and *P*–O stretching vibration, respectively. The peaks at 976 and 742 cm^{-1} are attributed to asymmetrical and symmetrical stretching vibration of *P*–*O*–P, respectively. The peaks at 686 and 505 cm^{-1} are due to asymmetrical and symmetrical deformation vibration of PO_3^-, respectively [35–37].

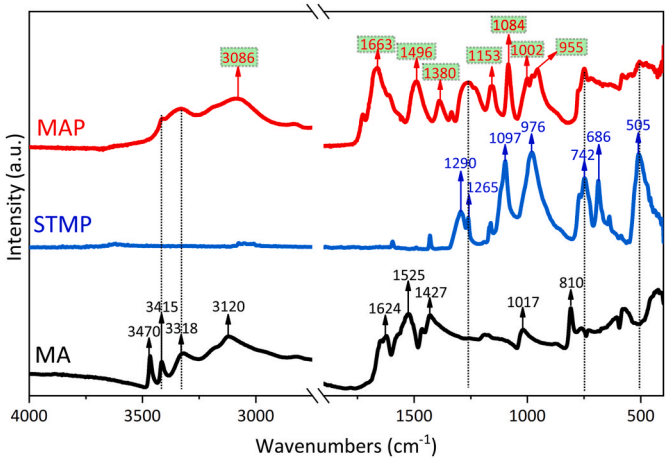

Fig. 2. FTIR spectra of MAP, STMP and MA.

Compared with MA and STMP, some of their characteristic peaks can be observed in the FTIR spectrum of MAP. And some new peaks are observed confirming the formation of hydrogen bonding between MA and trimetaphosphoric acid. The peaks at 3086, 1663, 1496, 1380 and 1084 cm^{-1} in MAP are corresponded to red-shift of hydrogen bonding between NH_2, NH_2 in-plane deformation, C═N, *C*–N and *P*–O stretching vibrations, respectively, due to the hydrogen bonding between MA and trimetaphosphoric acid. And the peak at 1153 cm^{-1} is ascribed to *P*–*O*–H–N hydrogen bonding between –NH_2 and trimetaphosphoric acid [35]. All this information confirms supramolecular structure of MAP.

As shown in Fig. 3, the ^{31}P NMR and ^{1}H NMR spectra further reveal the chemical structure of MAP. Only one signal of P atom is observed at −22.7 ppm in MAP, and one signal of P atom at −21.4 ppm is also shown in STMP (Fig. 3a) [38,39]. It is reported that the STMP ring can be opened in the presence of strong alkaline medium [40], resulting in the appearance of several signals in ^{31}P NMR spectrum. However, the only one signal of P atom in MAP indicates that the STMP ring is preserved during the formation of MAP. The chemical shift of P atom moved from −21.4 to −22.7 ppm in MAP is probably due to the conjugation effect from the introduction of MA ring.

Fig. 3b shows the ^{1}H MAS NMR spectrum of MAP and the results from quantitative deconvolution are plotted simultaneously. As

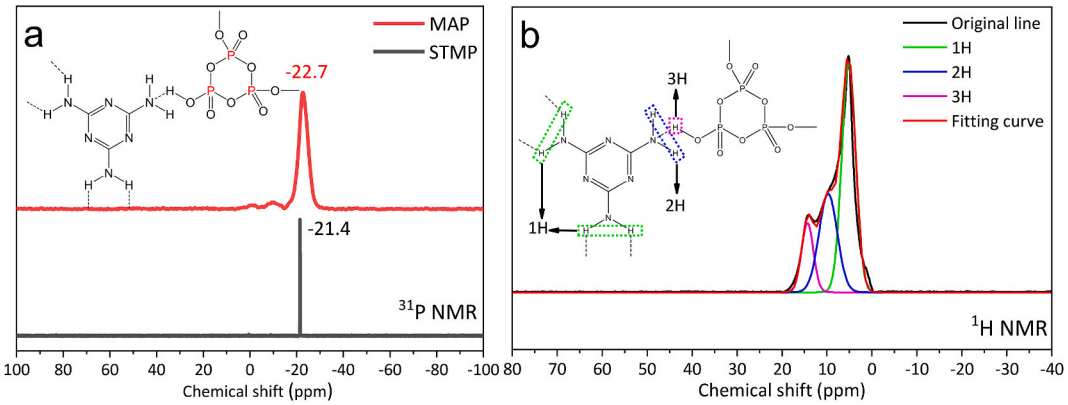

Fig. 3. ^{31}P NMR spectra of MAP and STMP (a). ^{1}H NMR and its deconvoluted spectra of MAP (b).

demonstrated, three signals of H protons can be identified clearly. The peak centered at 14.3 ppm is assigned to *P–O*–H–N hydrogen bonding, while the peaks at 9.6 and 5.2 ppm are attributed to two H protons in *P–O*–H–NH_2- and four H protons in two –NH_2 groups, respectively. The ratio of integral area about these three peaks is calculated to 4:2:1, which accurately corresponds to three kinds of H atom in the chemical structure of MAP (Fig. 3b). The ^{31}P NMR and ^{1}H NMR spectra give further evidence of the hydrogen bonding between two rings and the chemical structure of MAP.

The XRD traces of MA, STMP and MAP are shown in Fig. 4a. The MA diffractogram exhibits 6 peaks at 13.1°, 17.7°, 21.6°, 26.2°, 28.8° and 29.8° corresponding to (−101), (−111), (210), (−301), (−311) and (310) planes (JCPDS card No: 24–1654). The peaks of STMP at 13.5°, 17.8°, 23.2°, 26.3° 29.5°, 32.5° and 35.4° can be indexed to the (011), (111), (002), (220), (041), (231), and (013) planes (JCPDS card No: 72–1628) [41]. The XRD trace of MAP shows completely new reflection peaks indicating a new crystal structure.

The MAP crystal structure is refined with XRD trace by Accerlys from 5° to 30° (Fig. 4b). The powder refinement parameters are: R_{wp} = 6.64%, R_p = 16.53% (Fig. 4c). The MAP is triclinic with space group P1, a = 9.9644 Å, b = 11.6121 Å, c = 12.1757 Å, and α = 117.6702°, β = 95.4161°, γ = 77.7482°. The peaks at 9.1°, 12.2°, 16.4°, 18.8°, 24.7°, and 27.4° are referred to (100), (101), (11–2), (102), (2–12) and (212) planes (Fig. 4a). The calculated density (1.6842 g/cm^3) corresponds well with the experimental density (1.7950 g/cm^3). The crystallographic index file of MAP can be seen in Supporting **Information**.

Fig. 5 shows SEM, TEM and AFM images of MAP. The SEM image (Fig. 5a) of MAP crystal exhibits an obvious layered structure with ribbon shape. From EDS analysis (Fig. 5b) of the selected area in SEM image, the contents of C, N, O and P elements of MAP fit well with the theoretical values of MAP ($C_9N_{18}O_9P_3H_{21}$). The TEM image (Fig. 5c) shows semitransparent ribbons, indicating the thickness of the crystal nanoribbon of MAP is below 100 nm. Further thickness detection is carried out by AFM, as shown in Fig. 5d. The selected MAP sheet exhibits three stages with a total thickness of 10 nm. And the second and third stages have the same thickness at about 2 nm, indicating that the basal thickness of MAP crystal nanoribbon is about 2 nm. The bottom layer is about 6 nm due to the layer stacking. The above results provide sufficient evidence that MAP is a new type of 2D material.

3.2. *The thermal stability of MAP*

To study the thermal degradation behavior of MAP, STMP and MA, TGA is carried out in a nitrogen atmosphere from 40 °C to 800 °C, as shown in Fig. 6. The temperature of 5 wt % mass loss ($T_{5\%}$), taken as the onset temperature, and the fraction of residues remaining at 800 °C are recorded. And the temperatures of maximum mass loss rates are obtained from the DTG curves (Fig. 6b). $T_{5\%}$ of MAP and MA are 137 and 260 °C, respectively. The lower $T_{5\%}$ of MAP can be ascribed to dehydration of *P–O*–H–N hydrogen bonding between MA and trimetaphosphoric acid. Moreover, the residue of MAP (30.4%) is 20 times higher than MA (1.5%) at 800 °C due to the carbonization reaction between MA and trimetaphosphoric acid.

The DTG curves (Fig. 6b) point out that no peak is shown in STMP. Only one decomposition step is presented in MA (313 °C). However, there are three decomposition steps in MAP. The first step is attributable

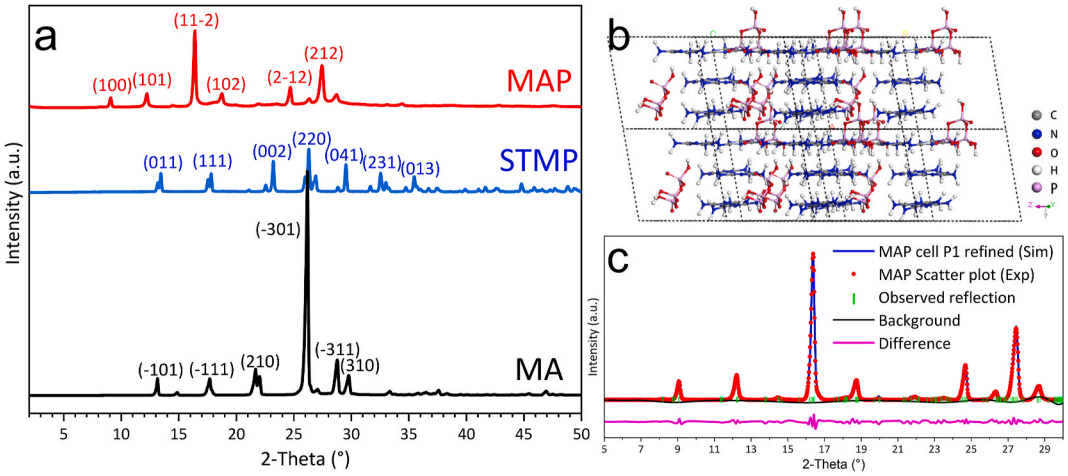

Fig. 4. XRD traces of MAP, STMP and MA (a). Scheme of MAP crystal structure (b). Simulated and experimental XRD traces of MAP, and their difference (c).

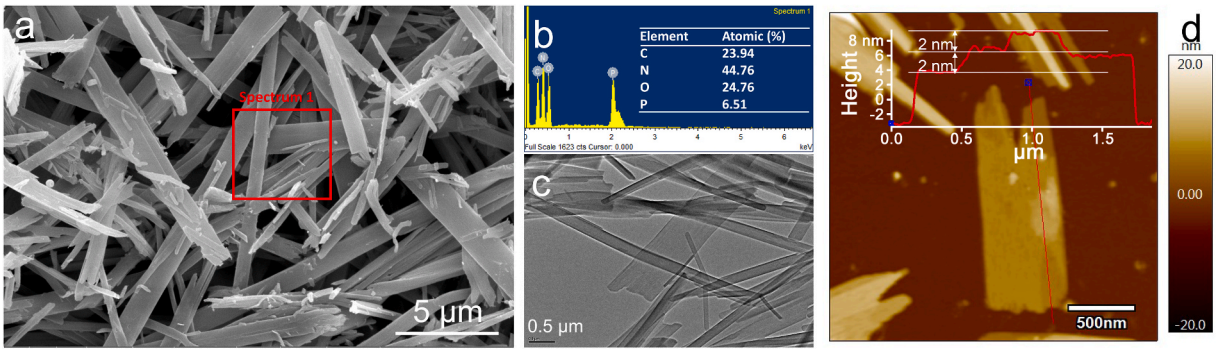

Fig. 5. SEM image of MAP (a). EDS analysis (b) of the selected area of SEM image. Inset: the elemental composition of selected area. TEM (c) and AFM images (d) of MAP, the inset is height profile along the red line. (For interpretation of the references to colour in this figure legend, the reader is referred to the Web version of this article.)

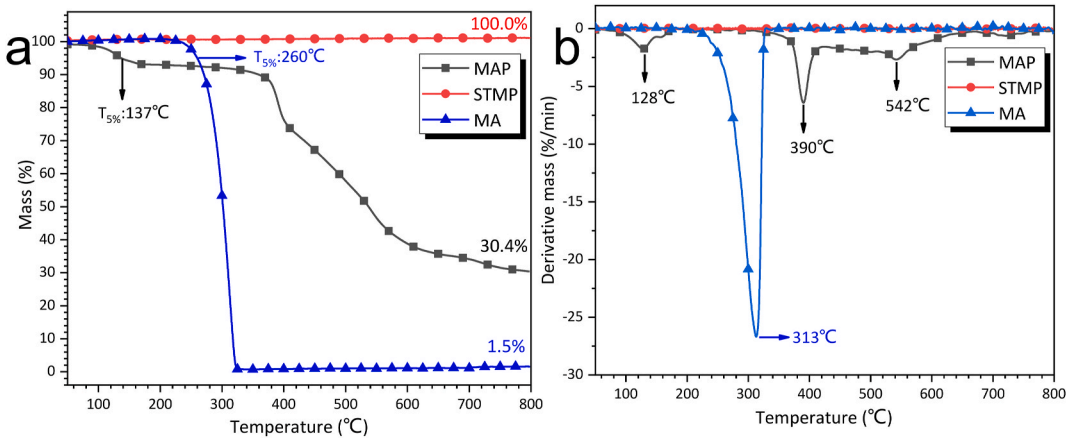

Fig. 6. TGA (a) and DTG curves (b) of MAP, STMP, and MA.

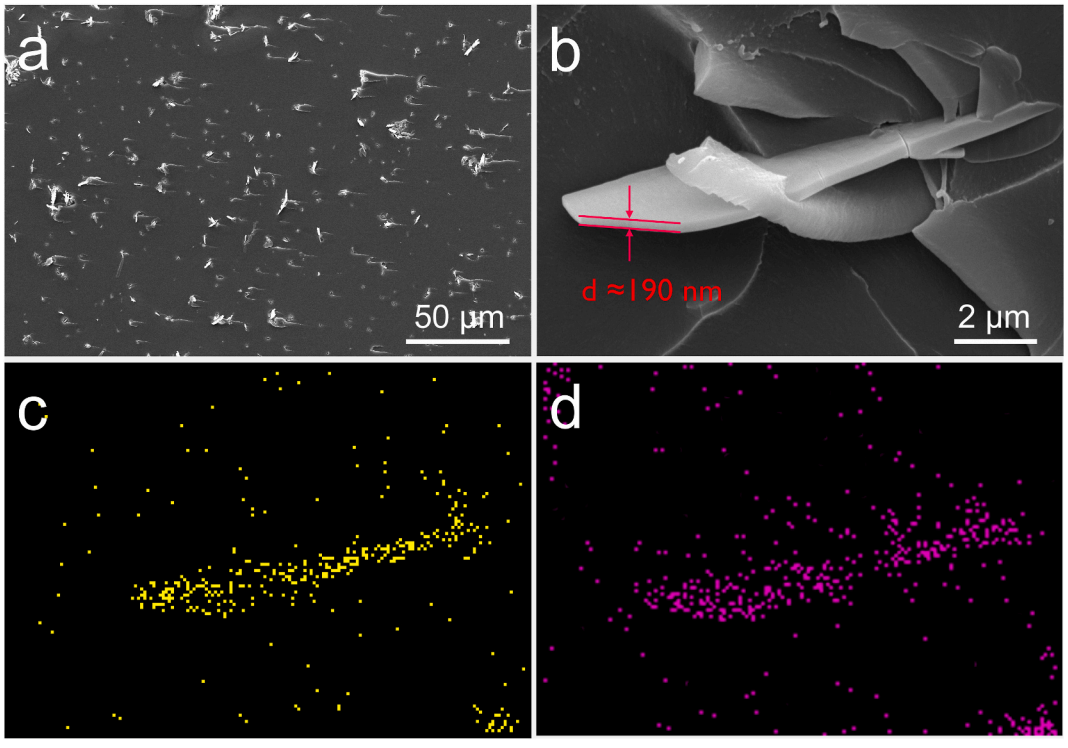

Fig. 7. SEM images of the brittle fracture surfaces of EP-MAP-4% at different magnification (a, b), and corresponding N and P elemental mappings (c, d) of Fig. 7b.

to the dehydration between MA and trimetaphosphoric acid (128 °C), and the second step is due to the char formation between MA and trimetaphosphoric acid rings (390 °C). The third step can be related to the loss of phosphoric acid fragments (542 °C) [17].

3.3. Morphologies of the EP-MAP composites

The cryofracture surface of EP-MAP-4% composite is observed by SEM, as shown in Fig. 7. Apparently, the MAP sheets are uniformly distributed in the EP matrix without obvious aggregation (Fig. 7a). From the high magnification SEM image of EP-MAP-4% (Fig. 7b), the MAP sheet with thickness around 190 nm is closely embedded in EP, showing the good interfacial interactions between two materials. Furthermore, the elemental mappings (Fig. 7c and d) for Fig. 7b demonstrate that N and P elements are intensively and uniformly distributed on MAP sheet, implying the integrality of MAP sheets during the preparation of EP-MAP composite.

3.4. Thermal stability of EP-MAP composites

As observed in Fig. 8 and Table 2, EP and EP-MAP composites all exhibit one step thermal degradation (Fig. 8a). Compared with $T_{5\%}$ of EP (365.0 °C), the $T_{5\%}$ of EP-MAP composites are all decreased with the increasing of MAP, which are 344.8, 343.5, 335.1, 330.2 °C for EP-MAP-1%, EP-MAP-2%, EP-MAP-3% and EP-MAP-4%, respectively. The lower $T_{5\%}$ of EP-MAP composites can be likely ascribed to the catalysis of phosphate for thermal decomposition of EP [42]. The residue at 800 °C ($R_{800°C}$) of EP is only 12.9%, whereas all EP-MAP composites show higher $R_{800°C}$ values. The $R_{800°C}$ is increased gradually with the increasing of MAP content. Moreover, the $R_{800°C}$ of EP-MAP-4% is increased by 9.1% with only 4% MAP addition, indicating the good char formation between MAP and EP.

The temperature of max mass loss rate (T_{max}) and max mass loss rate (MLR) of EP are 405.8 °C, and −17.7%/min, respectively (Fig. 8b). Both T_{max} and MLR of EP-MAP composites are decreased with the increasing of MAP content due to carbonization reaction between MAP and EP. The glass-transition temperatures (Tg) of EP and EP-MAP composites are listed in Table 2. The Tg of EP is 184 °C (Fig. 8c). The addition of 1% or 2% of MAP has no effect on Tg for EP. The slight decreasing of Tg for EP-MAP-3% and EP-MAP-4% is due to the good dispersion of MAP, acting as internal plasticization agent [43].

3.5. Flame retardancy of EP-MAP composites

The fire behaviors of EP-MAP composites are surveyed using LOI and UL-94 tests. The results are shown in Fig. 9a. EP is a flammable polymer with LOI at 23.0%. Interestingly, with 1% MAP, the LOI value of EP-MAP composite can be increased to 27.1%, indicating significantly improved flame retardancy. With the increasing of MAP content, the LOI values of EP-MAP composites are increased and finally reaches 30% for EP-MAP-4%. The 1% and 2% MAP addition cannot enable EP to achieve any rating in UL-94 test, while EP containing 3% MAP achieves V-1 rating without dripping. And V-0 rating can be reached at 4% MAP addition, indicating that EP-MAP-4% has the best flame retardancy among all samples. The EP-MAP-4% sample is almost undamaged after UL-94 test (Fig. 9b) and shows expanded and self-supporting char after LOI test (Fig. 9c).

Table 2
TGA, DTG and DSC data for EP and EP-MAP composites.

EP Samples	TGA		DTG		DSC
	$T_{5\%}$ (°C)	$R_{800°C}$ (%)	T_{max} (°C)	MLR (%/min)	Tg (°C)
EP	365.0	12.9	405.8	−17.7	184.0
EP-MAP-1%	344.8	17.4	391.7	−15.5	184.0
EP-MAP-2%	343.5	20.2	391.5	−14.2	184.0
EP-MAP-3%	335.1	21.8	386.7	−12.7	183.8
EP-MAP-4%	330.2	22.0	385.4	−12.5	182.0

Cone calorimeter tests are carried out to further investigate the fire performance. The heat release rate (HRR), total heat release (THR), smoke production rate (SPR), total smoke production (TSP), CO production rate (COP), and CO_2 production rate (CO_2P) are shown in Fig. 10, and corresponding data are summarized in Table 3, including time to ignition (TTI), peak of HRR (pHRR), time to pHRR (T_{pHRR}), fire growth index (FGI), fire performance index (FPI), peak of SPR (pSPR), peak of COP (pCOP), peak of CO_2P (pCO_2P), and the char residue (CR).

As shown in Table 3, the TTI of EP is 45 s, and all EP-MAP composite show slightly decreased TTI. This behavior is probably ascribed to the release of volatiles evolved by the catalysis of MAP for EP decomposition. The pHRR of EP is 1076 kW/m^2, and all EP-MAP composites show lower peak intensity (Fig. 10a). EP-MAP-1%, EP-MAP-2% and EP-MAP-3% exhibit similar pHRR values, which are 710, 688, and 672 kW/m^2, respectively. However, the pHRR of EP-MAP-4% can be greatly decreased to 370 kW/m^2 (65.6% reduction compared with that of pure EP), indicating a significant increasing in flame retardancy for epoxy. The THR values of EP-MAP-1% and EP-MAP-2% are almost same with that of pure EP (Fig. 10b), which are all around 90 MJ/m^2. EP-MAP-3% and EP-MAP-4% show the obviously decreased THR at about 72.9 MJ/m^2, due to carbonization reaction between MAP and EP according to oxygen consumption. FGI and FPI are two parameters to evaluate the fire growth. The lower FGI and higher FPI mean the better flame retardancy of sample. Compared with EP and other samples, the lowest FGI value and the highest FPI value of EP-MAP-4% exhibit the minimum fire hazard. These results suggest that protective and rigid char are formed on the burning surface of EP-MAP composites, which can inhibit the further combustion of EP.

The fatal atmosphere from the combustion of polymer account for the vast majority of fire fatalities. Therefore, it is necessary to reduce the production of smoke and toxic gases. Compared with EP, the evident decreasing of pSPR values is all shown in EP-MAP composites (Fig. 10c). Especially, the pSPR of EP-MAP-4% is significantly decreased to 0.16

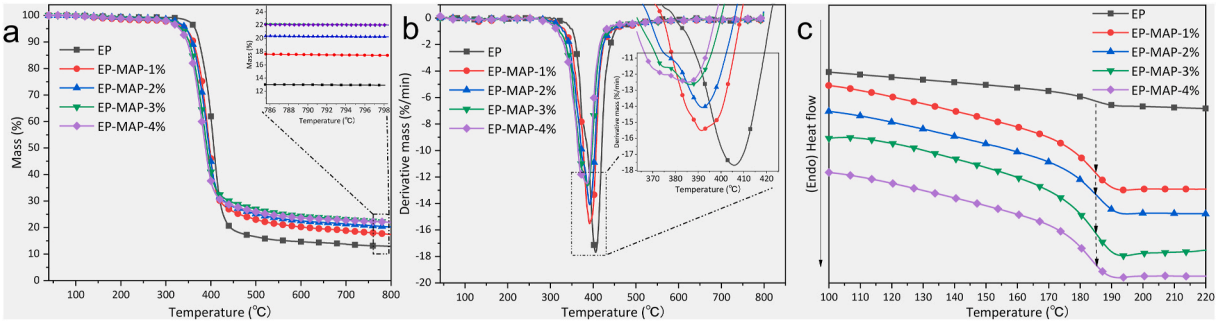

Fig. 8. TGA (a), DTG (b) and DSC (c) of EP and EP-MAP composites. The inset images show the blowup of TGA from 785 to 800 °C, and that of DTG from 363 to 425 °C, respectively.

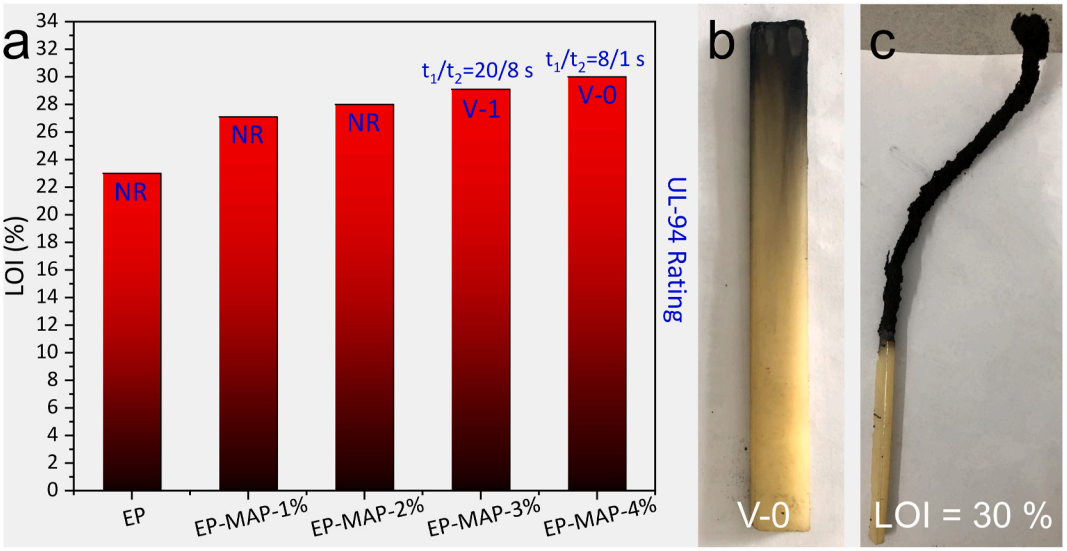

Fig. 9. LOI and UL-94 test results for EP and EP-MAP composites (a). Digital photos of EP-MAP-4% after the UL-94 (b) and LOI tests (c).

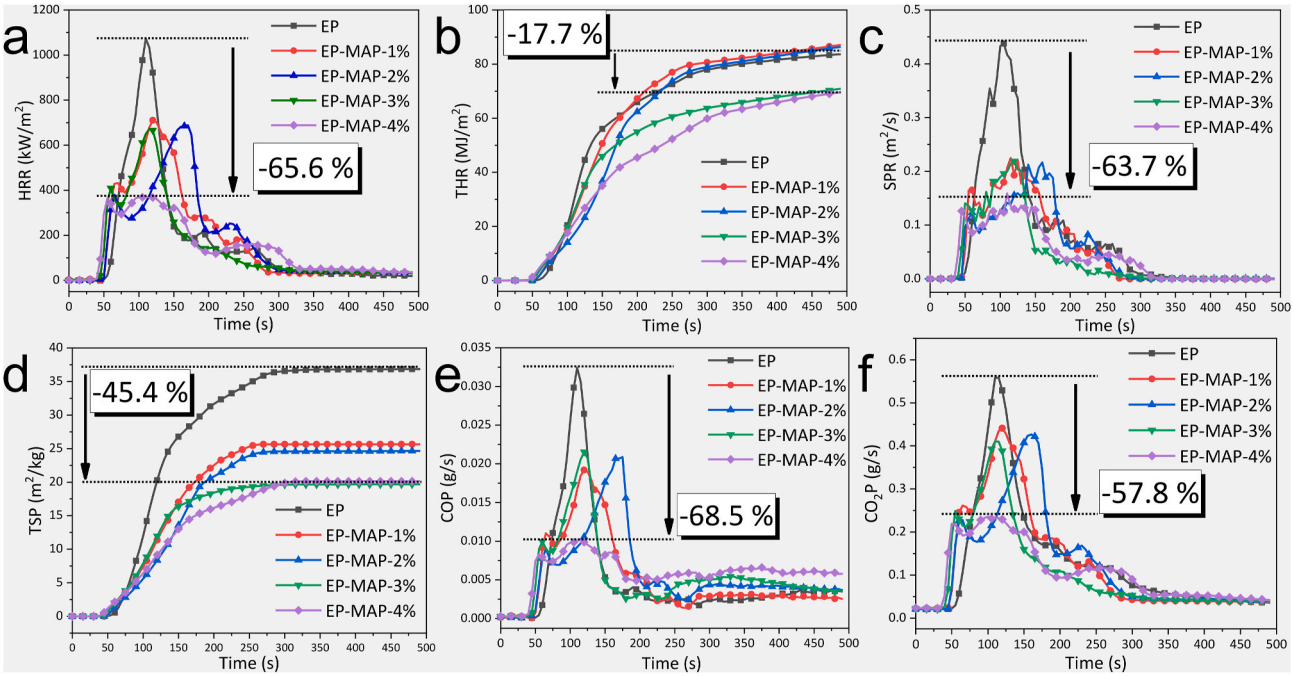

Fig. 10. Cone calorimeter curves of EP-MAP composites: (a) HRR curves; (b) THR curves; (c) SPR curves; (d) TSP curves; (e) COP curves; (f) CO_2P curves.

m^2/s (63.7% reduction compared with that of EP). TSP curves is shown in Fig. 10d. Compared with EP (36.9 m^2/kg), the addition of 1% and 2% MAP can reduce the TSP values to 25.6 and 24.7 m^2/kg, respectively. And the TSP of EP-MAP-4% is only 20.1 m^2/kg, decreased by 45.4%. In addition, the dynamic curves of COP and CO_2P have similar trendy with HRR curves, as shown in Fig. 10e and f. Compared with EP, the pCOP and pCO_2P of EP-MAP-4% can be decreased by 68.5% and 57.8%, respectively. Moreover, the CR of EP-MAP-4% are dramatically increased to 24.0% compared with that of pure EP (7.1%), indicating that more combustion intermediate products are kept in the condensed phase [44]. Above on, these EP-MAP composites perform well in suppressing smoke due to their strong ability to generate the high-quality and intumescent char layers, and strong evidence are provided by the morphology and chemical structures of the char.

3.6. Char morphologies

Digital photos of char for pure EP and EP-MAP composites are shown in Fig. 11 The thickness of char is written in red on the top. Pure EP is almost burnt out after combustion (Fig. 11a, a1), remaining little char at the edge. A cone of char is formed with thickness at 3 cm for EP-MAP-1% (Fig. 11b, b1). With the increasing of MAP addition, the expanded char becomes more cuboid, compact and solid. And the thickness is changed to 3 and 4 cm for EP-MAP-2% (Fig. 11c, c1) and EP-MAP-3% (Fig. 11d, d1), respectively. With 4% of MAP addition, the thickness of EP-MAP-4% char is extremely boosted to 8 cm (Fig. 11e, e1), which is the highest among all samples. The highly intumescent and compact char layer of EP-MAP-4% composite can perform good physical barrier for thermal, fuel and oxygen conductivity, effectively reducing heat release and inhibiting the release of toxic smoke during combustion.

Table 3
Cone calorimeter data of EP-MAP composites.

Samples	EP	EP-MAP-1%	EP-MAP-2%	EP-MAP-3%	EP-MAP-4%
TTI (s)	45 ± 2	43 ± 1	43 ± 3	42 ± 1	41 ± 2
pHRR (kW/m^2)	1076 ± 22	710 ± 25	688 ± 19	672 ± 21	370 ± 20
THR (MJ/m^2)	88.6 ± 2.1	90.8 ± 1.7	89.9 ± 2.2	74.1 ± 1.9	72.9 ± 1.8
FGI	9.78 ± 0.28	5.92 ± 0.20	4.05 ± 0.31	5.84 ± 0.34	3.22 ± 0.33
FPI	0.042 ± 0.002	0.061 ± 0.003	0.063 ± 0.003	0.063 ± 0.002	0.111 ± 0.004
pSPR (m^2/s)	0.44 ± 0.06	0.22 ± 0.05	0.22 ± 0.08	0.22 ± 0.03	0.16 ± 0.04
TSP (m^2/kg)	36.9 ± 2.3	25.6 ± 2.1	24.7 ± 1.8	19.7 ± 1.5	20.1 ± 1.6
pCOP (g/s)	0.032 ± 0.005	0.019 ± 0.004	0.021 ± 0.007	0.022 ± 0.004	0.010 ± 0.006
pCO$_2$P (g/s)	0.56 ± 0.04	0.44 ± 0.03	0.43 ± 0.05	0.41 ± 0.07	0.24 ± 0.08
CR (%)	7.1 ± 0.7	12.2 ± 0.8	13.4 ± 0.6	13.4 ± 0.8	24.0 ± 1.1

The microstructure of EP-MAP-4% char is then inspected by SEM (Fig. 12). The char (Fig. 12d) can be divided into three regions: the exterior (a and a1), middle (b and b1) and bottom parts (c and c1). The exterior char is thin and porous, and the holes are distributed on the surface with circle layered rough microchannels inside, shown in Fig. 12a. And char fragments are connected by fibrous strips (Fig. 12a). These porous chars can play physical barrier, and the rough microchannels can decrease diffusion rate of gas from inner to surface [45]. However, many gas bubbles with diameter at 100 μm are shown on the middle part, and interestingly, most of them are like deflated balloons with a smooth char film on the surface (Fig. 12b). As shown in Fig. 12b, the morphology of char film is smooth and glossy, but the char inside is rough. The char film may be carbon-containing phosphorus oxynitride composite after combustion [46], which can restrain the pyrolysis products released and eventually cause a large amount of bubbles [47,48]. Many small bubbles with diameter at 0.5 μm are emerged on the surface of bottom char layer (Fig. 12c and c1), and the other areas around bubbles are thick, compact, and continuous without any cracks. This phenomenon shows that the upper two parts can effectively insulate the heat, resulting in the presence of initial bubble and lower degree of thermal degradation for the bottom. In conclusion, this triple-parts protective char can be one of main reasons for its good suppression of heat and smoke during combustion.

3.7. Chemical structure of chars

The chemical structure of different parts in EP-MAP-4% char is then analyzed by XPS, as displayed in Fig. 13. The main elements detected in the wide-scan XPS spectra are C, N, O and P (Fig. 13a). From exterior to bottom part, the content of O element is gradually decreased but that of C element is increased, indicating the outside-in reduction of pyrolysis and oxidation degrees. The N and P contents in exterior part are much higher than other two parts, probably exhibiting the stronger *P*–N effect.

The C 1s XPS spectra (Fig. 13b) show three types of carbon with different chemical states: 284.8 eV (C–C), 286.2 eV (C–O), and 288.7 eV (N═C–N) [44,49,50]. The peak-fitting data and respective areas are shown in Table 4. From exterior part to bottom part, the intensity of *C*–C bond is increased, meanwhile, the intensity of oxidized carbon bonds (*C*–O) is decreased toward the interior of char, which further proof the effective thermal oxidative resistance of intumescent char layer.

The N 1s XPS spectra (Fig. 13c) are deconvoluted into three peaks, represented by several bonds, which are 399.1 eV (C═N–C), 400.7 eV (*P*–N), and 402.1 eV (*N*–H) [46,51,52]. As shown in Table 4, the intensity of C═N–C bond is decreased from exterior part to bottom part, meanwhile, the middle part shows the largest content of *P*–N and the fewest content of *N*–H. The high content of C═N–C and *N*–H bonds in exterior part are probably due to the pyrolysis and ring rearrangement of MAP, and MA rings can be gasified and released during degradation. The higher *P*–N content in middle and bottom parts indicates a better *P*–N effect, which generates many aromatic crosslinked char structures containing P and N elements, such as phosphorus oxynitride, phosphoramide, and phosphazene [46].

3.8. Evolved gaseous products analysis of EP composites

The evolved gaseous products during the thermal degradation of EP and EP-MAP-4% composites are analyzed by TGA-FTIR, shown in Fig. 14. The 3D spectra of EP-MAP-4% composite (Fig. 14b) is significantly different from that of pure EP (Fig. 14a). And several pyrolysis gaseous products are identified by the FTIR spectra at their maximum rate of thermal degradation (Fig. 14c). The characteristic peaks of gaseous products shown in EP spectrum appear at 3650 cm^{-1}, 3150-2800 cm^{-1}, 2350 cm^{-1}, 2190 cm^{-1}, 1740 cm^{-1}, 1670-1400 cm^{-1} and 1170 cm^{-1}, which are assigned to water, hydrocarbons, CO_2, CO, carbonyl compounds, aromatic compounds and ether, respectively [49,53]. However, the spectrum of EP-MAP-4% contains few characteristic peaks, and only CO_2 peak and weak carbonyl compound peak are detected, indicating that more volatilized intermediate compounds during the thermal degradation are catalyzed into solid char, and these intact char layers can strongly retard the escape of gaseous products. In addition, the spectra of aromatic compounds (Fig. 14d) and

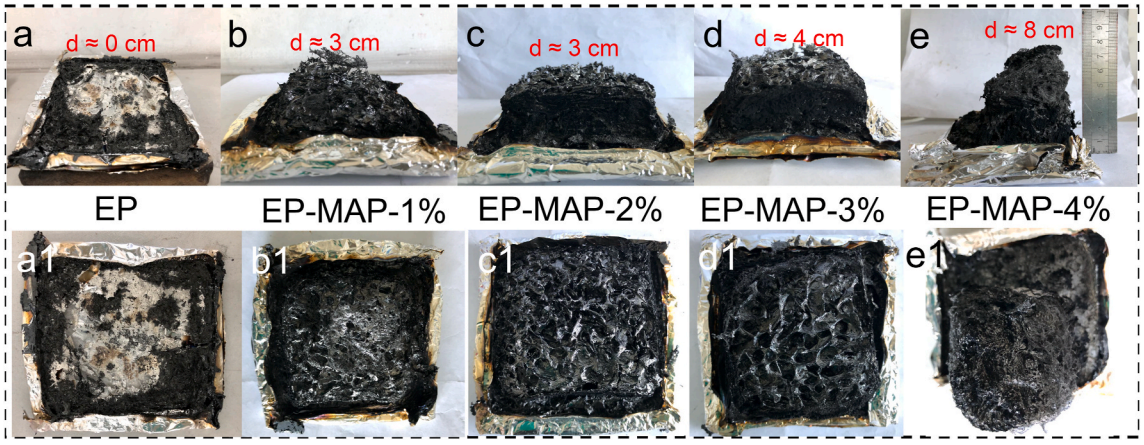

Fig. 11. Digital photographs of char from side view (a–e) and top view (a1~e1) of EP and EP-MAP composites after cone calorimeter tests.

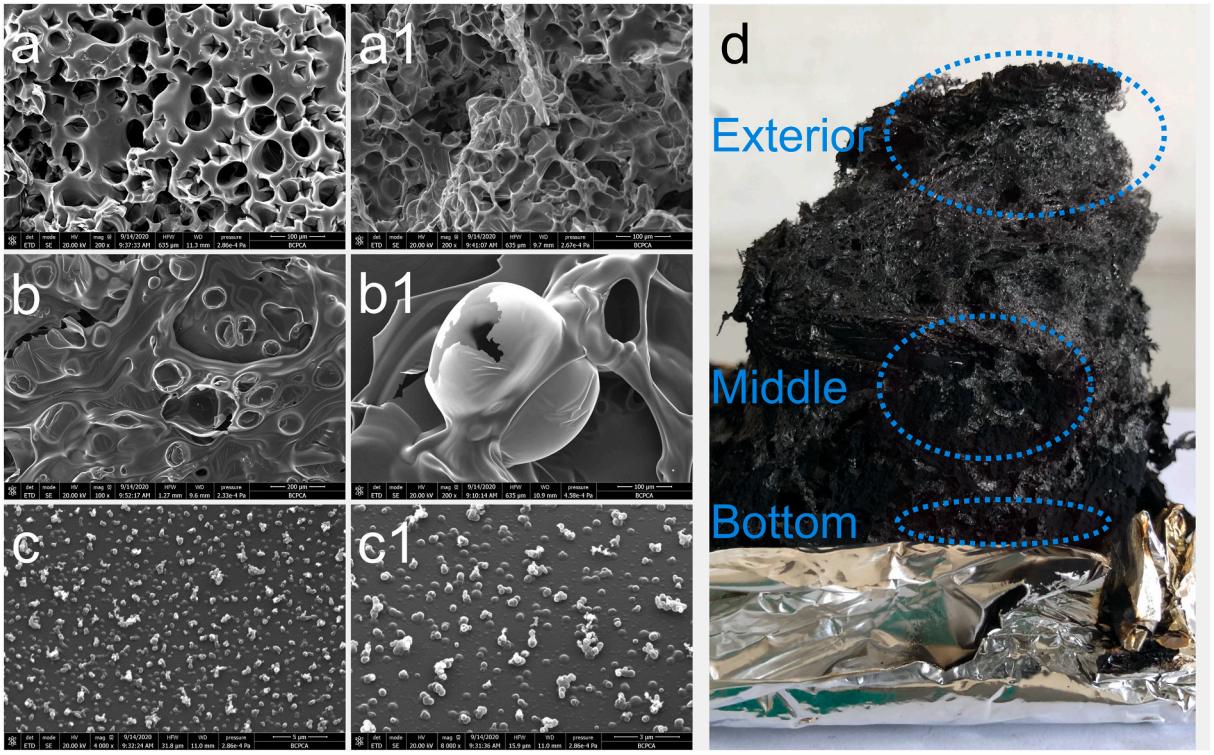

Fig. 12. SEM images of exterior (a and a1), middle (b and b1) and bottom parts (c and c1) char for EP-MAP-4%. The corresponding digital photograph (d).

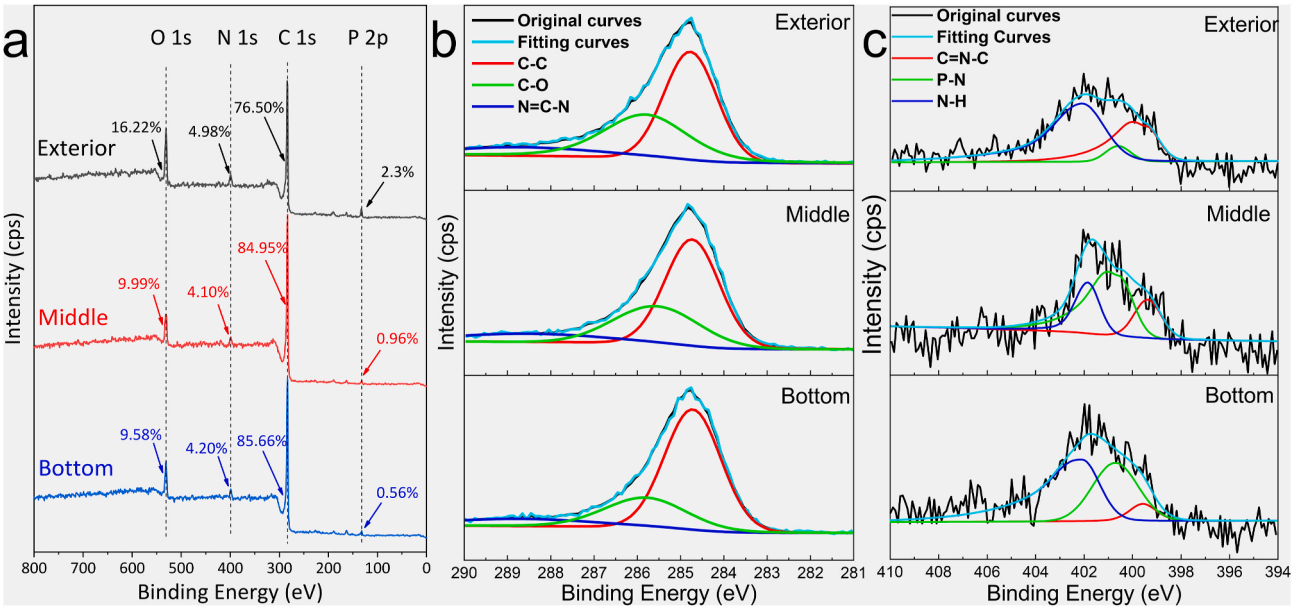

Fig. 13. XPS spectra of different parts of char for EP-MAP-4% (a). C 1s XPS spectra (b) and N 1s XPS spectra (c) of different parts.

hydrocarbons (Fig. 14e) produced during thermal degradation are displayed. The EP-MAP-4% exhibits much lower emissions than pure EP during the whole thermal degradation, indicating the strong suppression of smoke and thereby improving the fire safety.

3.9. The analysis of flame retardancy mechanism

According to TGA analysis of MAP, cone calorimeter results and char analysis of EP-MAP composite, a possible flame retardancy mechanism is draw in Fig. 15. In EP-MAP composite, MAP sheets are uniformly dispersed in EP matrix without aggregation. During the combustion, the endothermic condensation of *P–O*–H–N hydrogen bonding between two rings could lead to the formation of phosphoramide and water (step ①). The water and some of gasified MA rings can dilute the flammable gas diffusion and provokes the numerous rising bubbles, promoting the formation of intumescent char. Meanwhile, the ring-opening and random scission reactions (step ②) occur at higher temperatures, and the produced acidic phosphate fragment could act as acid source for catalytic dehydrogenation and char formation. Moreover, part of phosphorus-oxygen fragments is released to gas phase, which promotes

Table 4
Peak-fitting data for C 1s and N 1s XPS spectra for EP-MAP-4% char with different parts.

Kinds of bonds	Binding energy (eV)	Area for respective bonds (%)		
		Exterior	Middle	Bottom
C–C	284.8	51.8	56.5	63.4
C–O	286.2	34.4	30.9	24.5
N=C–N	288.7	13.8	12.6	12.1
C=N–C	399.1	32.3	19.3	7.3
P–N	400.7	6.4	55.5	36.1
N–H	402.1	61.3	25.2	56.6

the increasing of oxygen content in the char. As the combustion proceeds further, ring rearrangement reactions (step ③) could occur, leading to the generation of heterocycle containing P, N, and O elements, and many aromatic crosslinked char structures containing these heterocycles during the EP combustion can be formed (step ④). Finally, the stable, intumescent char mandate a tortuous pathway for flammable gas diffusion, and slows down the rate of heat and mass transfer, leading to the great flame retardancy.

3.10. Mechanical properties and dielectric properties of EP-MAP composites

The bending strength, strain at break and bending modulus of EP-MAP composites are shown in Fig. 16a. The bending strength, strain at break and bending modulus of pure EP are 96.9 MPa, 3.6% and 1763 MPa respectively. Three mechanics indexes of EP-MAP composites are all increased. For bending strength, EP-MAP-1% and EP-MAP-2% are relatively similar, which are 118.3 and 119.1 MPa, respectively. And with the increasing of MAP content, EP-MAP-3% and EP-MAP-4% show the higher bending strength values, which are 132.7 and 148.0 MPa, respectively. The strain at break value is gradually increased from EP-MAP-1% to EP-MAP-3%, which finally achieve the highest value at 8.6%. However, the strain at break value of EP-MAP-4% is decreased to 6.9%, which is close to that of EP-MAP-2% (6.8%). The bending modulus values of EP-MAP-1%, EP-MAP-2%, and EP-MAP-3% are also similar, which are 2770, 2807 and 2742 MPa, respectively. But EP-MAP-4% shows the highest bending modulus at 3389 MPa, indicating the best mechanical properties among EP-MAP samples. Compared with pure EP, the enhanced mechanical properties of EP-MAP composite can be due to the high aspect ratio and surface area of MAP, and the uniform dispersion between EP and MAP.

The low dielectric constant (ε') and dielectric loss (tan δ) values are required for insulating materials nowadays because of the increasing of operating frequency for electronic devices [12,54]. As shown in Fig. 16b, the dielectric constant of all EP-MAP composites is much lower than that of pure EP from 10^3 to 10^7 Hz, and EP-MAP-1% shows the lowest values. The dielectric constant is increased slightly with the increasing of MAP content. Moreover, similar tendency is shown for dielectric loss curve (Fig. 16c). The dielectric loss of all EP-MAP composites is lower than pure EP when the frequency is above 10^4, and

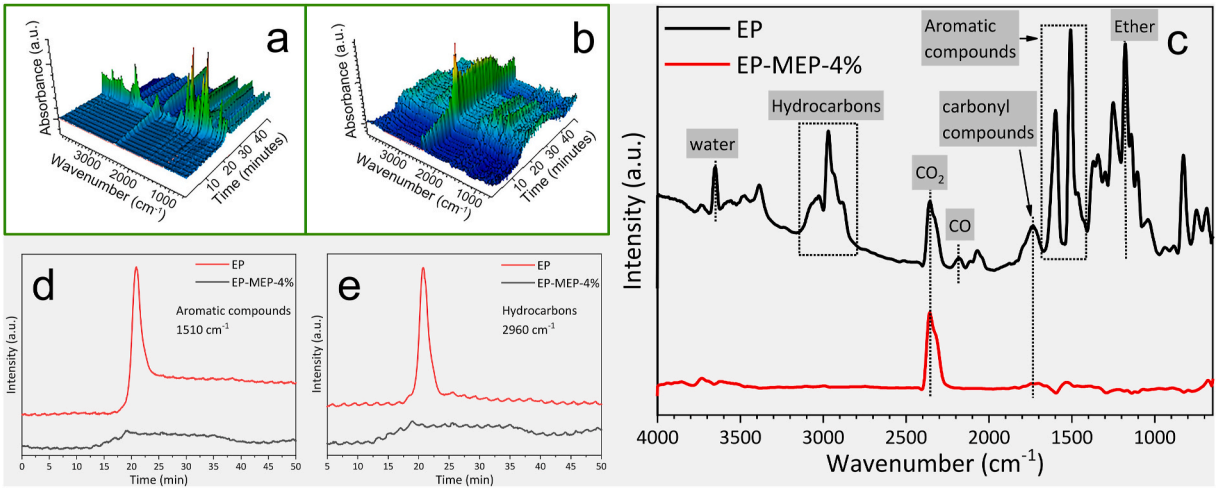

Fig. 14. TGA-FTIR spectra of EP and EP-MAP-4% composites: 3D spectra of EP (a) and EP-MAP-4% (b), FTIR spectra of pyrolysis products at maximum decomposition rates (c), the absorbance of typical volatile products: aromatic compounds (d) and hydrocarbons (e).

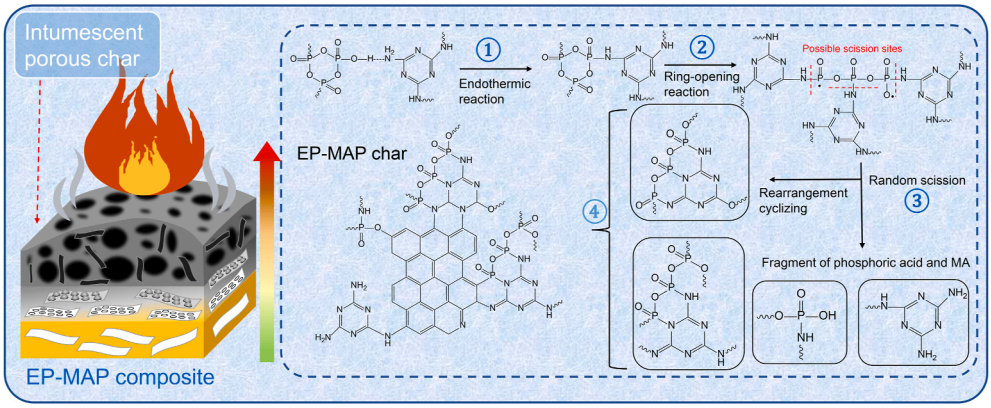

Fig. 15. Scheme of flame retardancy mechanism for MAP.

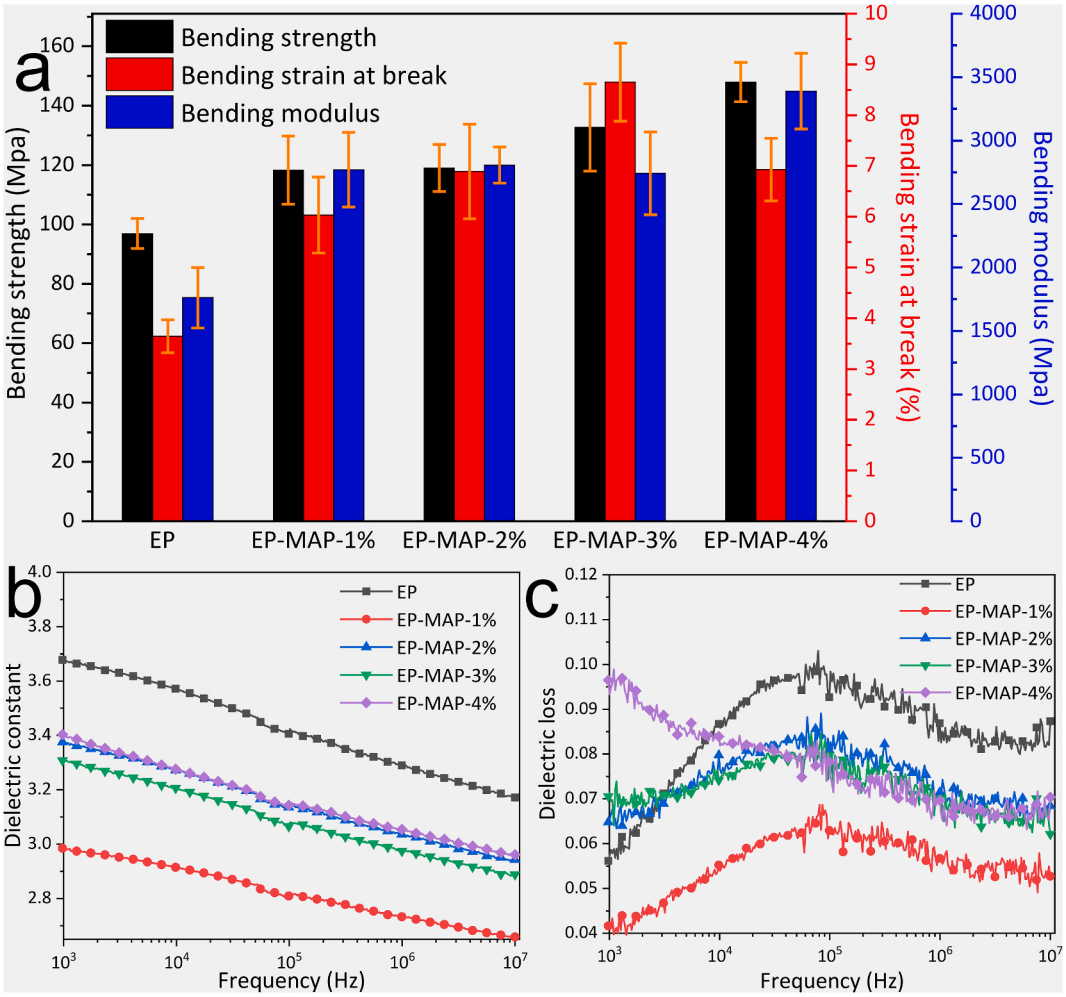

Fig. 16. Mechanical properties (a), dielectric constant curves (b) and dielectric loss curves (c) of EP and EP-MAP composites.

EP-MAP-1% also have the lowest dielectric loss values from 10^3 to 10^7 Hz. The low dielectric constant and dielectric loss values of EP-MAP composites could be attributed to an inhibition of the polarization-related charge carrier movement by the uniform dispersion of MAP in EP, which is beneficial for the application in the electronics field.

4. Conclusions

We synthesize a completely new 2D supermolecule flame retardant (MAP) using MA and STMP within acid environment. MAP layers with a thickness of 2 nm are formed by 3:1 combination of MA and STMP rings connected via intermolecular hydrogen bonding (*P*–*O*–H–N), and its crystal structure is identified and simulated. And MAP exhibits a pretty high thermal stability and three thermal degradation steps. Then EP-MAP composite is prepared. MAP can be uniformly distributed in EP without obvious aggregation. The thermal stability of EP-MAP is increased and the Tg values show little changes. The flame retardancy of EP-MAP is also increased. With 0.60% P content and 1.64% N content, EP-MAP-4% can achieve 30.0% of LOI value and UL-94 V-0 rating. Meanwhile, in cone test, the pHRR is significantly reduced by 65.6% and SPR, COP and CO_2P is largely decreased by 63.7%, 68.5%, and 57.8%, respectively. The residual expanded char is compact and solid, and the thickness is boosted to 8 cm for EP-MAP-4%. The microstructure of char is then fully inspected by SEM. XPS analysis of char indicates the typical *P*–N effect and the decreasing of oxidized carbon bonds from exterior toward interior. The TGA-FTIR spectra further confirm the high suppression of smoke release of EP-MAP. A possible flame retardancy mechanism of MAP is then proposed. In addition, the mechanical and dielectric properties of EP-MAP are also significantly enhanced. MAP, as an "all-in-one" IFR, can effectively improve the collision probability between acid source, charring agent and blowing agent, thereby effectively increasing the flame retardancy. Meanwhile, the controllable 2D supermolecule structure endows MAP with good dispersion in EP. With slight addition of MAP, EP-MAP composites show outstanding flame retardancy, mechanical and dielectric properties.

CRediT authorship contribution statement

Peifan Qin: Methodology, Investigation, Writing – original draft. **Deqi Yi:** Conceptualization, Software, Writing – review & editing. **Jianwei Hao:** Data curation, Supervision. **Xinming Ye:** Data curation, Visualization. **Ming Gao:** Validation, Investigation. **Tinglu Song:** Methodology, Visualization.

Declaration of competing interest

The authors declare that they have no known competing financial interests or personal relationships that could have appeared to influence the work reported in this paper.

Acknowledgements

The work was partially supported by the National Natural Science

Foundation of China under grant number 51303012. Thanks to Mr. Lewis Morton for polishing our paper.

Appendix A. Supplementary data

Supplementary data to this article can be found online at https://doi.org/10.1016/j.compositesb.2021.109269.

References

[1] Jian R-K, Lin X-B, Liu Z-Q, Zhang W, Zhang J, Zhang L, Li Z, Wang D-Y. Rationally designed zinc borate@ZIF-8 core-shell nanorods for curing epoxy resins along with low flammability and high mechanical property. Compos B Eng 2020;200:108349.

[2] Zeng L, Liu X, Chen X, Soutis C. π - π interaction between carbon fibre and epoxy resin for interface improvement in composites. Compos B Eng 2021;220:108983.

[3] Wang X, Guo W, Song L, Hu Y. Intrinsically flame retardant bio-based epoxy thermosets: a review. Compos B Eng 2019;179:107487.

[4] Zhang Y, Yan H, Feng G, Liu R, Yang K, Feng W, Zhang S, He C. Non-aromatic Si, P, -containing hyperbranched flame retardant on reducing fire hazards of epoxy resin with desirable mechanical properties and lower curing temperature. Compos B Eng 2021:109043.

[5] Zhu M, Liu L, Wang Z. Iron-phosphorus-nitrogen functionalized reduced graphene oxide for epoxy resin with reduced fire hazards and improved impact toughness. Compos B Eng 2020;199:108283.

[6] Yang S, Huo S, Wang J, Zhang B, Wang J, Ran S, Fang Z, Song P, Wang H. A highly fire-safe and smoke-suppressive single-component epoxy resin with switchable curing temperature and rapid curing rate. Compos B Eng 2021;207:108601.

[7] Huo S, Yang S, Wang J, Cheng J, Zhang Q, Hu Y, Ding G, Zhang Q, Song P, Wang H. A liquid phosphaphenanthrene-derived imidazole for improved flame retardancy and smoke suppression of epoxy resin. ACS Applied Polymer Materials 2020;2(8):3566–75.

[8] Huo S, Song P, Yu B, Ran S, Chevali VS, Liu L, Fang Z, Wang H. Phosphorus-containing flame retardant epoxy thermosets: recent advances and future perspectives. Prog Polym Sci 2021;114:101366.

[9] Huo S, Yang S, Wang J, Cheng J, Zhang Q, Hu Y, Ding G, Zhang Q, Song P. A liquid phosphorus-containing imidazole derivative as flame-retardant curing agent for epoxy resin with enhanced thermal latency, mechanical, and flame-retardant performances. J Hazard Mater 2020;386:121984.

[10] He W, Song P, Yu B, Fang Z, Wang H. Flame retardant polymeric nanocomposites through the combination of nanomaterials and conventional flame retardants. Prog Mater Sci 2020;114:100687.

[11] Xue Y, Shen M, Zeng S, Zhang W, Hao L, Yang L, Song P. A novel strategy for enhancing the flame resistance, dynamic mechanical and the thermal degradation properties of epoxy nanocomposites. Mater Res Express 2019;6(12):125003.

[12] Ye X, Li J, Zhang W, Yang R, Li J. Fabrication of eco-friendly and multifunctional sodium-containing polyhedral oligomeric silsesquioxane and its flame retardancy on epoxy resin. Compos B Eng 2020;191:107961.

[13] Hou Y, Xu Z, Chu F, Gui Z, Song L, Hu Y, Hu W. A review on metal-organic hybrids as flame retardants for enhancing fire safety of polymer composites. Compos B Eng 2021;221:109014.

[14] Yang H, Guan Y, Ye L, Wang S, Li S, Wen X, Chen X, Mijowska E, Tang T. Synergistic effect of nanoscale carbon black and ammonium polyphosphate on improving thermal stability and flame retardancy of polypropylene: a reactive network for strengthening carbon layer. Compos B Eng 2019;174:107038.

[15] Guo W, Yu B, Yuan Y, Song L, Hu Y. In situ preparation of reduced graphene oxide/DOPO-based phosphonamidate hybrids towards high-performance epoxy nanocomposites. Compos B Eng 2017;123:154–64.

[16] Sai T, Ran S, Guo Z, Yan H, Zhang Y, Wang H, Song P, Fang Z. Transparent, highly thermostable and flame retardant polycarbonate enabled by rod-like phosphorous-containing metal complex aggregates. Chem Eng J 2021;409:128223.

[17] Deqi Y, Rongjie Y. Ammonium polyphosphate/montmorillonite nanocompounds in polypropylene. J Appl Polym Sci 2010;118(2):834–40.

[18] Qin P, Yi D, Xing J, Zhou M, Hao J. Study on flame retardancy of ammonium polyphosphate/montmorillonite nanocompound coated cellulose paper and its application as surface flame retarded treatment for polypropylene. J Therm Anal Calorim 2021. https://doi.org/10.1007/s10973-020-10427-1.

[19] Fang F, Huo S, Shen H, Ran S, Wang H, Song P, Fang Z. A bio-based ionic complex with different oxidation states of phosphorus for reducing flammability and smoke release of epoxy resins. Composites Communications 2020;17:104–8.

[20] Zhao L, Sui X-L, Li J-Z, Zhang J-J, Zhang L-M, Huang G-S, Wang Z-B. Supramolecular assembly promoted synthesis of three-dimensional nitrogen doped graphene frameworks as efficient electrocatalyst for oxygen reduction reaction and methanol electrooxidation. Appl Catal, B 2018;231:224–33.

[21] Sai T, Ran SY, Guo ZH, Fang ZP. Fabrication of a La-based metal organic framework and its effect on fire safety and thermal stability of polycarbonate. Acta Polym Sin 2019;50(12):1338–47.

[22] Whitesides G, Mathias J, Seto C. Molecular self-assembly and nanochemistry: a chemical strategy for the synthesis of nanostructures. Science 1991;254(5036):1312–9.

[23] Jun Y-S, Lee EZ, Wang X, Hong WH, Stucky GD, Thomas A. From melamine-cyanuric acid supramolecular aggregates to carbon nitride hollow spheres. Adv Funct Mater 2013;23(29):3661–7.

[24] Dong H, Yuan B, Qi C, Li K, Shang S, Sun Y, Chen G, Zhang H, Chen X. Preparation of piperazine cyanurate by hydrogen-bonding self-assembly reaction and its application in intumescent flame-retardant polypropylene composites. Polym Adv Technol 2020;31(5):1027–37.

[25] Fang F, Ran S, Fang Z, Song P, Wang H. Improved flame resistance and thermo-mechanical properties of epoxy resin nanocomposites from functionalized graphene oxide via self-assembly in water. Compos B Eng 2019;165:406–16.

[26] Yang W, Song L, Hu Y, Lu H, Yuen RKK. Enhancement of fire retardancy performance of glass-fibre reinforced poly(ethylene terephthalate) composites with the incorporation of aluminum hypophosphite and melamine cyanurate. Compos B Eng 2011;42(5):1057–65.

[27] Shi Y, Liu C, Duan Z, Yu B, Liu M, Song P. Interface engineering of MXene towards super-tough and strong polymer nanocomposites with high ductility and excellent fire safety. Chem Eng J 2020;399:125829.

[28] Zhao M, Yi D, Camino G, Frache A, Yang R. Interdigitated crystalline MMT-MCA: preparation and characterization. Polym Adv Technol 2018;29(1):22–9.

[29] Shang S, Yuan B, Sun Y, Chen G, Huang C, Yu B, He S, Dai H, Chen X. Facile preparation of layered melamine-phytate flame retardant via supramolecular self-assembly technology. J Colloid Interface Sci 2019;553:364–71.

[30] Qi C, Yuan B, Dong H, Li K, Shang S, Sun Y, Chen G, Zhan Y. Supramolecular self-assembly modification of ammonium polyphosphate and its flame retardant application in polypropylene. Polym Adv Technol 2020;31(5):1099–109.

[31] Zhang L, Yi D, Hao J. Poly (diallyldimethylammonium) and polyphosphate polyelectrolyte complexes as an all-in-one flame retardant for polypropylene. Polym Adv Technol 2020;31(2):260–72.

[32] Zhang L, Yi D, Hao J. Poly(diallyldimethylammonium) and polyphosphate polyelectrolyte complex as flame retardant for char-forming epoxy resins. J Fire Sci 2020;38(4):333–47.

[33] Costa L, Camino G. Thermal behaviour of melamine. J Therm Anal 1988;34(2):423–9.

[34] Jones WJ, Orville-Thomas WJ. The infra-red spectrum and structure of melamine. Trans Faraday Soc 1959;55:203–10.

[35] Shifu W. Fourier transform infrared spectrometer. Beijing: Chemical Industry Press; 2005.

[36] Gunter GC, Craciun R, Tam MS, Jackson JE, Miller DJ. FTIR and31P-NMR spectroscopic analyses of surface species in phosphate-catalyzed lactic acid conversion. J Catal 1996;164(1):207–19.

[37] Ogden JS, Williams SJ. The identification of molecular NaPO3 and NaPO2 by matrix isolation IR spectroscopy. J Chem Phys 1980;73(4):2007–8.

[38] Sang Y, Prakash O, Seib PA. Characterization of phosphorylated cross-linked resistant starch by 31P nuclear magnetic resonance (31P NMR) spectroscopy. Carbohydr Polym 2007;67(2):201–12.

[39] Sojka SA, Wolfe RA. Analysis of commercial sodium tripolyphosphates by phosphorus-31 Fourier transform nuclear magnetic resonance spectrometry. Anal Chem 1978;50(4):585–7.

[40] Lack S, Dulong V, Picton L, Le Cerf D, Condamine E. High-resolution nuclear magnetic resonance spectroscopy studies of polysaccharides crosslinked by sodium trimetaphosphate: a proposal for the reaction mechanism. Carbohydr Res 2007;342(7):943–53.

[41] Li L, Chen Y, Guo X, Zhong B. Preparation of sodium trimetaphosphate and its application as an additive agent in a novel polyvinylidene fluoride based gel polymer electrolyte in lithium sulfur batteries. Polym Chem 2015;6(9):1619–26.

[42] Zhang W, He X, Song T, Jiao Q, Yang R. The influence of the phosphorus-based flame retardant on the flame retardancy of the epoxy resins. Polym Degrad Stabil 2014;109:209–17.

[43] Kiliaris P, Papaspyrides CD. Polymer/layered silicate (clay) nanocomposites: an overview of flame retardancy. Prog Polym Sci 2010;35(7):902–58.

[44] Wang Y, Li Z, Li Y, Wang J, Liu X, Song T, Yang X, Hao J. Spray-drying-assisted layer-by-layer assembly of alginate, 3-aminopropyltriethoxysilane, and magnesium hydroxide flame retardant and its catalytic graphitization in ethylene–vinyl acetate resin. ACS Appl Mater Interfaces 2018;10(12):10490–500.

[45] Zhao M, Yi D, Camino G, Frache A, Yang R. Interdigitated crystalline MMT–MCA in polyamide 6. RSC Adv 2017;7(2):861–9.

[46] Gaan S, Sun G, Hutches K, Engelhard MH. Effect of nitrogen additives on flame retardant action of tributyl phosphate: phosphorus–nitrogen synergism. Polym Degrad Stabil 2008;93(1):99–108.

[47] Hull TR, Kandola B. Fire retardancy of polymers: new strategies and mechanisms. Cambrige: RSC Publishing; 2009.

[48] Li J, Ou Y. The theory of flame retardancy. Beijing: Science Press; 2013.

[49] Zhang Z, Qin J, Zhang W, Pan Y-T, Wang D-Y, Yang R. Synthesis of a novel dual layered double hydroxide hybrid nanomaterial and its application in epoxy nanocomposites. Chem Eng J 2020;381:122777.

[50] Ran J, Ma TY, Gao G, Du X-W, Qiao SZ. Porous P-doped graphitic carbon nitride nanosheets for synergistically enhanced visible-light photocatalytic H2 production. Energy Environ Sci 2015;8(12):3708–17.

[51] Yung H, Shih PY, Liu HS, Chin TS. Nitridation effect on properties of stannous-lead phosphate glasses. J Am Ceram Soc 1997;80(9):2213–20.

[52] Xu S-H, Wang J-F, Valério A, Zhang W-Y, Sun J-L, He D-N. Activating Co nanoparticles on graphitic carbon nitride by tuning the Schottky barrier via P

doping for the efficient dehydrogenation of ammonia-borane. Inorg Chem Front 2021;8(1):48–58.

[53] Qiu S, Wang X, Yu B, Feng X, Mu X, Yuen RKK, Hu Y. Flame-retardant-wrapped polyphosphazene nanotubes: a novel strategy for enhancing the flame retardancy and smoke toxicity suppression of epoxy resins. J Hazard Mater 2017;325:327–39.

[54] Xu Y-J, Chen L, Rao W-H, Qi M, Guo D-M, Liao W, Wang Y-Z. Latent curing epoxy system with excellent thermal stability, flame retardance and dielectric property. Chem Eng J 2018;347:223–32.